

RESEARCH LETTER

10.1002/2016GL067954

Key Points:

- Sentinel-1 wide-swath mode can be used to compute along-track horizontal displacement within burst overlap regions
- Along-track and across-track interferometry on ascending and descending passes provide four different viewing geometries
- Validation with GPS data shows that all three components of surface displacement are resolved with subdecimetric accuracy

Correspondence to:

R. Grandin,
grandin@ipgp.fr

Citation:

Grandin, R., E. Klein, M. Métois, and C. Vigny (2016), Three-dimensional displacement field of the 2015 M_w 8.3 Illapel earthquake (Chile) from across- and along-track Sentinel-1 TOPS interferometry, *Geophys. Res. Lett.*, 43, doi:10.1002/2016GL067954.

Received 24 JAN 2016

Accepted 1 MAR 2016

Accepted article online 6 MAR 2016

Three-dimensional displacement field of the 2015 M_w 8.3 Illapel earthquake (Chile) from across- and along-track Sentinel-1 TOPS interferometry

R. Grandin¹, E. Klein^{2,3}, M. Métois⁴, and C. Vigny²

¹Institut de Physique du Globe de Paris, UMR 7154, Sorbonne Paris Cité, Université Paris Diderot, Paris, France,

²Laboratoire de Géologie, ENS, UMR 8538 CNRS, member of PSL-research university, Paris, France, ³Now at Institut Physique du Globe de Strasbourg, UMR 7516 CNRS, Université de Strasbourg/EOST, Strasbourg, France, ⁴Univ Lyon, Université Lyon 1, ENS de Lyon, CNRS, UMR 5276 LGL-TPE, Villeurbanne, France

Abstract Wide-swath imaging has become a standard acquisition mode for radar missions aiming at applying synthetic aperture radar interferometry (InSAR) at global scale with enhanced revisit frequency. Increased swath width, compared to classical Stripmap imaging mode, is achieved at the expense of azimuthal resolution. This makes along-track displacements, and subsequently north-south displacements, difficult to measure using conventional split-beam (multiple-aperture) InSAR or cross-correlation techniques. Alternatively, we show here that the along-track component of ground motion can be deduced from the double difference between backward and forward looking interferograms within regions of burst overlap. “Burst overlap interferometry” takes advantage of the large squint angle diversity of Sentinel-1 ($\sim 1^\circ$) to achieve subdecimetric accuracy on the along-track component of ground motion. We demonstrate the efficiency of this method using Sentinel-1 data covering the 2015 M_w 8.3 Illapel earthquake (Chile) for which we retrieve the full 3-D displacement field and validate it against observations from a dense network of GPS sensors.

1. Introduction

Since the pioneering contributions of the 1990s, monitoring of large-scale ground motion using interferometric synthetic aperture radar (InSAR) has made spectacular progress. Thanks to improvement of the phased array technology, advances in orbitography, increasing computational power as well as the launch of multiple civilian synthetic aperture radar (SAR) missions since the 2000s, a broad range of natural and anthropogenic processes can be routinely monitored today (see *Simons and Rosen* [2007] for a recent review). Among these processes, the InSAR technique has proved extremely valuable in mapping the displacement field induced by large plate boundary events, such as earthquakes or magmatic intrusions, especially in geographical areas where GPS measurements are lacking [e.g., *Peltzer et al.*, 1999; *Grandin et al.*, 2009].

One limitation of InSAR is that only the component of deformation in the sensor line of sight (LOS), i.e., the across-track component, can be resolved. Acquisitions from ascending and descending passes are usually combined to provide two different viewing geometries. Even so, due to the near-polar orbit of SAR satellites, resolution on the north-south component remains poor [*Wright et al.*, 2004].

Therefore, in complement to conventional InSAR, a number of signal processing techniques have been proposed to retrieve the horizontal component of displacement parallel to the satellite track. These methods, which rely either on the amplitude (incoherent cross correlation, also termed offset tracking [*Michel et al.*, 1999; *Fialko et al.*, 2001]) or on the phase (multiple-aperture InSAR, also termed split-beam interferometry [*Bechor and Zebker*, 2006; *Barbot et al.*, 2008; *Jung et al.*, 2009]), typically allow for resolving displacements exceeding $\sim 10\%$ of the azimuth pixel size. Hence, for classical Stripmap mode (azimuth pixel size of the order of a few meters), displacements greater than a few decimeters can be resolved. As a consequence, the resolution that can be achieved with such methods restricts their applicability to the study of intermediate to large earthquakes ($M_w > 6$).

Recent advances in SAR technology and processing have allowed for the emergence of a new generation of sensors entirely dedicated to wide-swath imaging. Wide-swath modes allow for global mapping

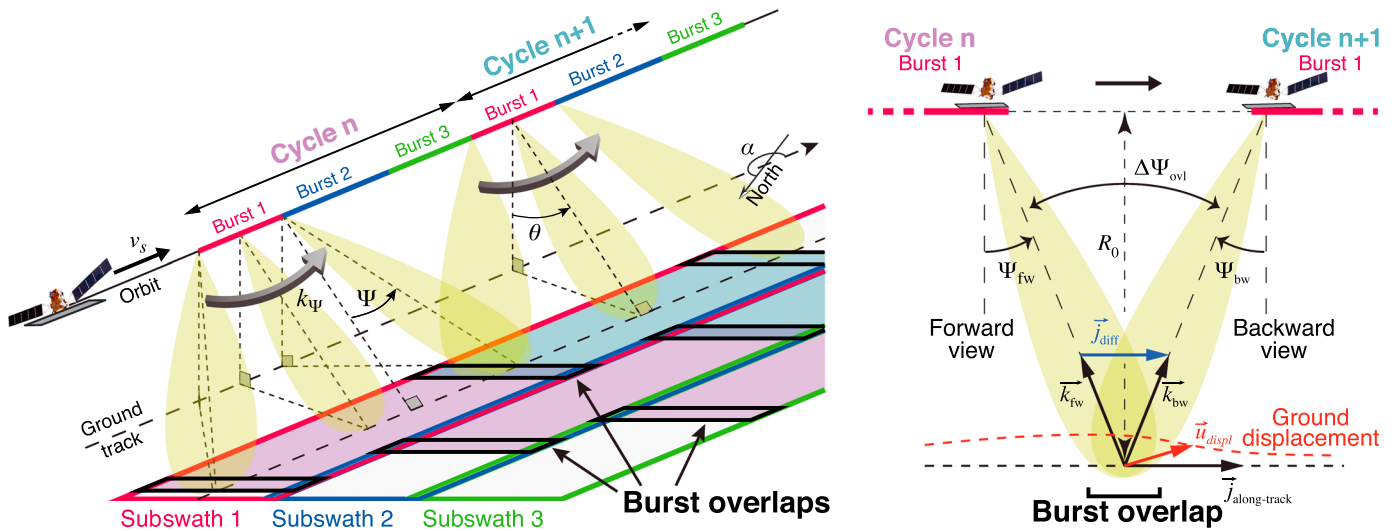


Figure 1. (left) Principle of TOPS imaging mode. (right) Squint angle diversity in burst overlap regions.

with an increased revisit frequency, as exemplified by the two satellites Sentinel-1 and ALOS-2, respectively operating TOPS and ScanSAR as standard acquisition modes. Unfortunately, the increase of the swath breadth by a factor of 3 to 5 comes at the expense of reduced azimuthal resolution by an equivalent factor. Trading azimuth resolution for increased swath width, hence shortened revisit interval, is arguably advantageous for studying large-scale tectonic deformation, whether coseismic, postseismic, or interseismic [e.g., Grandin *et al.*, 2015]. On the other hand, split-beam and offset-tracking techniques become limited to sensing along-track displacement exceeding ~ 50 cm, hence restricting their potential usefulness [Jung *et al.*, 2014].

Alternatively, we propose here to take advantage of wide-swath burst modes, especially TOPS, by applying along-track interferometry in regions where successive bursts overlap in the azimuth direction (Figure 1). This technique, whose original objective was to improve the coregistration of a slave image against its master [Scheiber and Moreira, 2000; Prats-Iraola *et al.*, 2012], is used here for another purpose. We show that burst overlap interferometry allows for resolving subtle motion along the azimuth direction. The technique is particularly efficient for Sentinel-1 TOPS data, as beam steering in azimuth provides an increased squint angle diversity within burst overlaps, hence a better resolution on horizontal motion compared to conventional split-beam interferometry applied to Stripmap or ScanSAR images.

In this paper, focusing on the case study of the Illapel earthquake (Chile, 16 September 2015, M_w 8.3), we use Sentinel-1 wide-swath data to retrieve the full 3-D surface displacement field. Independent measurements acquired by a continuous GPS network allow for validating the method and estimating its uncertainty.

2. Method

2.1. TOPS Along-Track Interferometry

Sentinel-1 is the first SAR mission to implement the TOPS mode as a standard acquisition mode for interferometry (Figure 1) [Torres *et al.*, 2012]. Similar to ScanSAR, an extended swath is achieved in TOPS mode by electronically steering the beam in elevation periodically so as to cover several adjacent subswaths (three in the case of Sentinel-1 “interferometric wide-swath” mode, IW) [De Zan and Guarnieri, 2006]. Each subswath is imaged in a succession of bursts, typically consisting of a thousand pulses. Because a given ground pixel is only illuminated during a fraction of the standard Stripmap mode synthetic aperture duration, the resulting azimuth bandwidth of burst modes, hence the achievable azimuth resolution, is decreased accordingly. On the other hand, the range properties of the images (bandwidth and resolution) are unchanged.

In ScanSAR mode, the beam angle with respect to zero-Doppler direction (also termed “squint” angle) is held fixed. In TOPS mode, a steady drift of the squint angle, from backward to forward, is introduced over the course of the burst transmission in order to broaden the size of the illuminated area in the azimuth direction (Figure 1, left). As a result, TOPS achieves improved image quality both in terms of phase (reduced azimuth

ambiguity) and amplitude (decreased “scalping” effect) [Meta *et al.*, 2008]. Nevertheless, both ScanSAR and TOPS require accurate burst synchronization to warrant sufficient azimuth spectral overlap for interferometry [Holzner and Bamler, 2002].

In wide-swath mode, a small overlap region occurs between the bursts to ensure that the final processed image will be devoid of any gap (Figure 1, left). In these “burst overlap regions,” ground pixels are observed twice from two slightly different angles or equivalently with two different Doppler centroid frequencies (Figure 1, right). In ScanSAR mode, this azimuth angular separation is limited by beam aperture, which usually does not exceed 0.25° . In TOPS mode, the Doppler centroid difference is much greater, as a direct consequence of the squinted view introduced by beam steering in azimuth. For Sentinel-1, the difference in squint angle is typically of the order of 1° , with overlap regions corresponding to $\sim 10\%$ of the burst length.

When processing TOPS data for interferometry, it is possible to take advantage of the slight difference in squint angles within overlap regions in order to retrieve the horizontal component of ground motion parallel to the satellite track. Akin to multiple aperture InSAR, a double difference of the phase within overlap regions is computed as follows (Figure 1, right): (1) calculate the interferogram using only the phase deduced from the forward view $\Delta\Phi_{fw}$, (2) calculate the interferogram in the backward view $\Delta\Phi_{bw}$, and (3) compute the difference between forward looking and backward looking interferograms $\Delta\Phi_{ovi} = \Delta\Phi_{fw} - \Delta\Phi_{bw}$ (see Appendix A for details). This technique will be thereafter referred to as “burst overlap interferometry.”

The final double-difference interferogram corresponds to the temporal variation of the difference in slant range from two slightly different squint angles. In observation scenarios devoid of any ground motion, the double-difference phase $\Delta\Phi_{ovi}$ only includes the effect of slight errors in coregistration between the master and slave images [Scheiber and Moreira, 2000]. Hence, this procedure is commonly used to refine coregistration during TOPS InSAR processing, a method known as “enhanced spectral diversity” (ESD) [e.g., Prats-Iraola *et al.*, 2012]. On the other hand, when significant ground motion has occurred between two acquisitions, phase jumps across burst boundaries in TOPS interferograms are diagnostic of horizontal ground motion along the satellite track [e.g., De Zan *et al.*, 2014; González *et al.*, 2015]. The double-difference procedure allows for directly measuring this phase difference on a pixelwise basis within overlap regions. Topographic and tropospheric contributions are largely cancelled by the double difference, which results in better phase quality than in the across-track interferogram.

2.2. Data Set

In order to map the 3-D displacement field of the 2015 $M_w 8.3$ Illapel earthquake, we use SAR data acquired by Sentinel-1A in IW TOPS mode. Images before the earthquake were acquired on 24 August 2015 and 26 August 2015 for the descending and ascending passes, respectively. Postearthquake acquisitions were performed on 17 September 2015 (+11 h after quake) and 19 September 2015 (+3 days). Interferograms are computed using the method of Grandin [2015], starting from level 1 single look complex products distributed by the European Space Agency (ESA). Precise orbits (<https://qc.sentinel1.eo.esa.int>) and Shuttle Radar Topography Mission 1-arc second DEM are used for orbital and topographic corrections. Azimuth phase deramping is calculated using precise coregistration derived from pixel offsets and further refined by means of ESD within burst overlaps [Prats-Iraola *et al.*, 2012; Grandin, 2015]. Interferograms are multilooked by a factor of 12 in range and 4 in azimuth, resulting in a ground pixel of ~ 60 m. Unwrapping is performed using the cut tree algorithm [Goldstein *et al.*, 1988] and corrected manually when necessary.

Azimuth displacements are retrieved using the burst overlap interferometry technique (see Appendix A for details). Flat Earth, topographic correction, and multilooking are applied to the forward and backward interferograms prior to computation of the double-difference interferogram [De Zan *et al.*, 2015]. A spatial coherence mask with a threshold of 0.4 is applied to discard unreliable phase values. Pixels are low-pass filtered using 1 km wide maximum likelihood estimator. Flattening of interferograms is performed by fitting a bilinear polynomial surface on the difference between, on the one hand, GPS measurements from a local geodetic network (S. Ruiz *et al.*, The seismic sequence of the 16 September 2005, Illapel $M_w 8.3$ earthquake, *Seismological Research Letters*, under review, 2016) projected onto the appropriate unit vector (along or across track) and, on the other hand, the nearest pixel in the interferogram. Finally, interpolation by a Laplacian operator is applied in order to fill the gaps between the bursts.

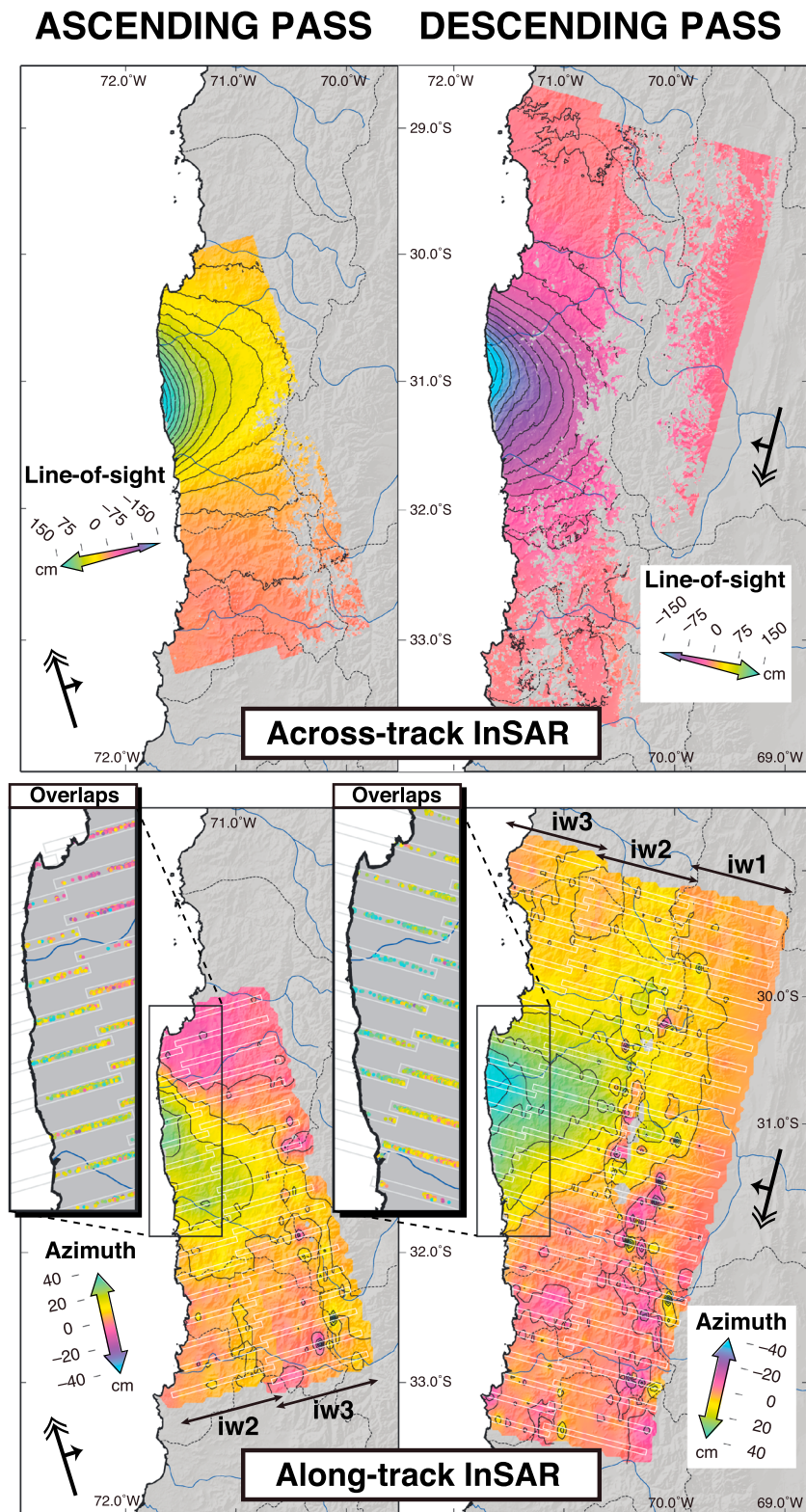


Figure 2. (top) Across-track and (bottom) along-track displacement field from Sentinel-1 InSAR. Note the different color scaling for across-track and along-track InSARs. The left and right panels of Figure 2 (top) correspond to ascending and descending passes, respectively. Double-headed arrow shows direction of flight of the platform. White rectangles in Figure 2 (bottom) indicate regions of burst overlaps. The along-track displacement field was filtered and interpolated between regions of bursts to produce a continuous displacement field. Insets show unfiltered double-difference phase prior to interpolation.

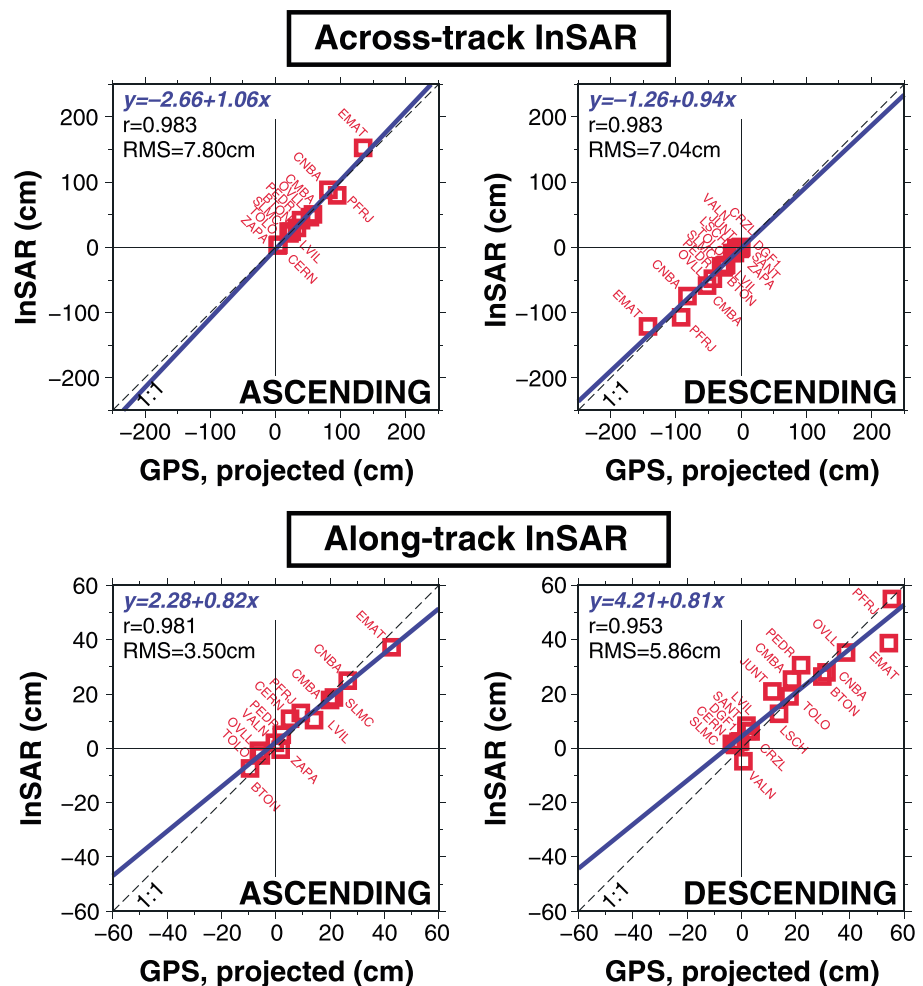


Figure 3. Linear regression between GPS and (top) across-track InSAR or (bottom) along-track InSAR. Left panels of Figure 3 (top and bottom) are for the ascending pass, and right panels of Figure 3 (top and bottom) are for the descending pass (same ordering as in Figure 2). Note the different scaling for across-track and along-track InSARs.

3. Results and Discussion

3.1. Along-Track InSAR

Across-track interferograms show a maximum line-of-sight displacement of ± 150 cm, picturing the semi-circular fringe pattern typical of subduction earthquakes in Chile [e.g., Pritchard *et al.*, 2006] (Figure 2, top). Displacement occurs exclusively away from the satellite in the descending pass and toward the satellite in the ascending pass. This is consistent with seaward motion reaching ≥ 1 m in the coastal area combined with moderate vertical displacement (within the range ± 50 cm) due to the offshore earthquake location. Furthermore, we notice that peak displacement in the descending across-track interferogram occurs ~ 30 km to the north of the peak in the ascending interferogram. This suggests that displacement vectors experience substantial rotation, either about a vertical or horizontal axis, at 31°S . However, as a result of the acquisition geometry of InSAR, the vertical and north-south components cannot be distinguished in the across-track interferograms. Hence, all the details of the actual ground displacement field cannot be restituted solely from these two across-track interferograms.

In contrast, along-track interferograms derived from the burst overlap interferometry technique show a more complex displacement pattern with both negative and positive displacements peaking at ± 40 cm (Figure 2, bottom). Displacements vary smoothly over distances exceeding ~ 20 km, which is twice the distance separating two consecutive burst overlap regions. This demonstrates that interpolation between burst overlaps did not lead to significant aliasing of the displacement field. Due to the near-polar orbit, along-track interferograms are strongly sensitive to the north-south component of motion, whereas across-track interferograms

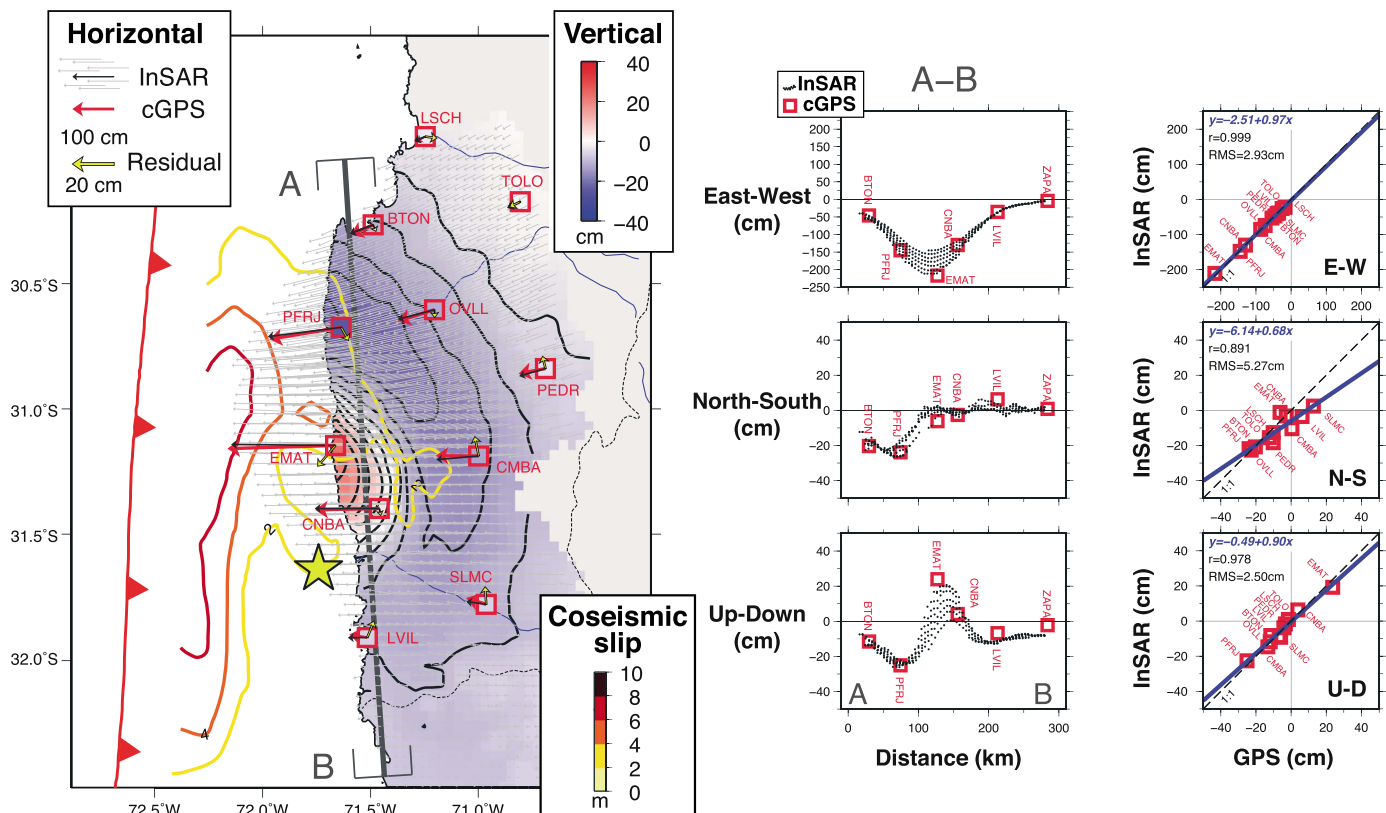


Figure 4. (left) Three-dimensional surface displacement reconstructed from Sentinel-1 InSAR. Red arrows show displacement at continuous GPS sites (cGPS), while color fill in red squares interior represents the vertical component of displacement from GPS (S. Ruiz et al., under review, 2016). Black arrows show displacement deduced from Sentinel-1 InSAR at locations of GPS benchmarks. Residuals are shown in yellow, with enhanced scaling. Grey arrows show horizontal displacement sampled on a regular grid. The colored grid in the background shows the vertical component of displacement on the same regular grid, with contours at 5 cm interval overlaid. Coseismic slip contours from the U.S. Geological Survey are shown for comparison (http://earthquake.usgs.gov/earthquakes/eventpage/us20003k7a#scientific_findefault). (middle) Transect showing comparison between Sentinel-1 InSAR and GPS. Location of the profile is shown in Figure 4 (left). East-west component (top), north-south component (middle), and vertical component (bottom). Sign convention is right-handed ENU. Note the different scaling for the east-west component. (right) Linear regression between Sentinel-1 InSAR and GPS displacements at GPS sites.

are least sensitive to this component. In the particular case of the Illapel earthquake, horizontal displacement occurs mostly trench normal, i.e., with an azimuth of 260°N. The ascending along-track interferogram, which is nearly insensitive to the trench-normal displacement, shows a sign reversal consistent with trench-parallel, southward motion in the north, shifting to trench-parallel, northward motion in the south. In the along-track descending interferogram, peak displacement occurs in the northern part, at 30.7°S, which is also compatible with a significant component of southward displacement in that area. These trench-parallel displacements are consistent with a radial, centripetal pattern of horizontal displacement vectors pointing toward the centroid of the earthquake. This effect is most pronounced toward the north and south edges of the main slip area, a feature that can be used to refine source models of the earthquake.

3.2. Comparison With GPS Data

Projection of GPS displacements in the line of sight (LOS) and along the direction of the satellite track allows for validating the accuracy of the interferometric products for across-track and along-track interferograms, respectively (Figure 3). This comparison yields a root-mean-square (RMS) residual of 7.8 cm and 7.0 cm for ascending and descending across-track interferograms, respectively. This residual is consistent with fluctuations caused by atmospheric turbulence, which usually reach 1–2 fringes in C-band interferograms in north-central Chile [Ducret, 2013]. Linear regression between across-track InSAR and GPS projected in the LOS shows an excellent mutual agreement, with a coefficient of correlation above 0.98 and a proportionality factor within 10% of unity.

For the along-track component of ground motion measured by burst overlap interferometry, the RMS is equal to 3.5 cm and 5.9 cm for ascending and descending geometries, respectively. This subdecimetric misfit is in

agreement with theoretical expectations (see Appendix A for details). The slope of the linear regression is close to 0.8 in either case. This value departs from unity, which may be due to bias on the slope determination imparted by misfits on the few points located in the area of maximum displacement along the coast (Figure 3). In particular, maximum misfit in the descending along-track interferogram chiefly occurs at site EMAT, which has recorded a peak trenchward (westward) displacement of 220 cm (Figure 3, lower-right panel). Due to instrument malfunction, the GPS-derived coseismic displacement at EMAT includes 2 days of postseismic displacement that is largely absent in the descending interferogram (postquake image acquired +11 h after main shock). Yet significant postseismic motion, likely resulting from rapid afterslip, is evident in time series from cGPS sites located along the coast (6–7 cm eastward displacement is recorded in the 24 h following the main shock at sites CMBA and PFRJ). Therefore, significant residual postseismic motion may explain part of the misfit at EMAT.

3.3. Three-Dimensional Displacement Field

The 3-D displacement field can be deduced from the four components of ground motion sensed by across- and along-track interferograms on both ascending and descending geometries (Figure 4). This is achieved by solving an overdetermined linear system involving three unknowns and four equations, consisting in the LOS and azimuth displacements in ascending and descending passes. The agreement between GPS- and InSAR-derived displacements is below 3 cm for the vertical and east-west components, which are best resolved. The RMS is only slightly higher (5.3 cm) for the north-south component, which would otherwise remain unresolved by standard across-track InSAR. The rotation of displacement vectors along the shoreline is well reproduced, as well as the shift from coastal subsidence to coastal uplift at 31.1°S. This change is consistent with vertical motion recorded by intertidal fauna (S. Ruiz et al., under review, 2016). Coseismic slip extending below the continent near the epicenter, and remaining offshore further to the north, explains this feature [Melgar et al., 2016; S. Ruiz et al., under review, 2016].

4. Conclusion

This study demonstrates the capability of the Sentinel-1 system, operating in wide-swath TOPS mode, to capture the full 3-D displacement field of large subduction earthquakes at subdecimetric accuracy for all three components. In the particular case of an earthquake where horizontal displacement is predominantly east-west and displacements vary smoothly, such as large subduction earthquakes in South America, Japan, or Cascadia, Sentinel-1 allows for quickly and exhaustively mapping surface displacement. For shallower and/or smaller earthquakes, the method may partly miss the variability of displacement over length scales smaller than 10 km, as along-track burst overlap interferometry is only practicable in burst overlap regions. Nevertheless, within burst overlap regions, the along-track component of displacement is available at dense spatial sampling and is not influenced by tropospheric phase screen. This is similar to having a densely spaced campaign GPS transect at disposal, which already represents a substantial improvement. Between these sparse burst overlap regions, conventional split-beam and/or offset-tracking can provide a background measurement, albeit with less accuracy [Jung et al., 2014; Scheiber et al., 2015]. Future development of agile SAR antennas and innovative acquisition modes, such as bidirectional SAR or SuperSAR, should provide two simultaneous squinted views with continuous spatial sampling [Mittermayer et al., 2013; Jung et al., 2015], thereby truly extending the InSAR technique toward full 3-D capability.

Appendix A: Along-Track Ground Displacement From TOPS Interferometry

A1. Principle of Burst Overlap Interferometry

In along-track double-difference burst overlap interferograms, the azimuth displacement Δx_{az} is proportional to the azimuth time shift induced by target displacement along the azimuth time axis Δt_{az} (or equally the azimuth misregistration) and to the difference in instantaneous Doppler frequency Δf_{ovl} between forward and backward views in the overlap region [Scheiber and Moreira, 2000]

$$\Delta\Phi_{ovl} = 2\pi\Delta f_{ovl}\Delta t_{az} = 2\pi\Delta f_{ovl}\frac{\Delta x_{az}}{\Delta x_s}\Delta t_s \quad (A1)$$

where Δt_s is the azimuth sampling and Δx_s is the azimuth pixel size. In TOPS wide-swath mode, the frequency difference Δf_{ovl} is the product of the effective Doppler rate K_t and the duration of a full TOPS cycle T_{cycle} [Prats-Iraola et al., 2012]

$$\Delta f_{ovl} = |K_t|T_{cycle} \quad (A2)$$

Table A1. Parameters of Sentinel-1 IW Data Used in This Study (Descending Pair)

Parameters	Values			
		1	2	3
Subswath				
Range ^a	R_o	829 km	879 km	933 km
Incidence angle ^a	θ	34°	39°	44°
Antenna steering rate	k_Ψ	1.59° s ⁻¹	0.98° s ⁻¹	1.40° s ⁻¹
Time separation between overlaps	$\Delta\eta_{ovl}$	0.80 s	0.96 s	0.82 s
Squint difference in overlap region	$\Delta\Psi_{ovl}$	1.28°	0.94°	1.15°
Doppler rate due to platform motion ^a	K_a	-2260 Hz	-2131 Hz	-2008 Hz
Doppler rate due to antenna steering ^a	K_s	7593 Hz	4679 Hz	6672 Hz
Doppler rate in focused SLC ^a	K_t	1742 Hz	1464 Hz	1544 Hz
Wavelength	λ		5.55 cm	
Platform heading (clockwise with respect to north)	α		-167.2°	
Platform velocity	v_s		7211 m s ⁻¹	
Azimuth sampling	Δt_s		0.002056 s	
Azimuth pixel size	Δx_s		14.07 m	
Burst cycle duration	T_{cycle}		2.75 s	

^aAt midrange.

The effective Doppler rate K_t results from the combination of the classical Doppler rate induced by platform motion K_a and the supplemental effect K_s induced by beam steering at a rate k_Ψ from the aft to the fore [De Zan and Guarnieri, 2006]

$$K_t = \frac{K_a K_s}{K_a - K_s} ; \quad K_a = -\frac{2v_s^2}{\lambda R_o} ; \quad K_s \approx \frac{2v_s}{\lambda} k_\Psi \quad (A3)$$

The same result can be deduced equivalently by considering the difference between line-of-sight (LOS) vectors for the two observation directions available in burst overlaps. The azimuth displacement is the projection of ground motion \vec{u}_{displ} onto the difference, within the overlap region, between the LOS vectors \vec{k}_{fw} and \vec{k}_{bw} of the forward interferogram and the backward interferogram, respectively (Figure 1b)

$$\begin{aligned} \Delta\Phi_{ovl} &= (\Delta\Phi_{fw} - \Delta\Phi_{bw}) = \frac{4\pi}{\lambda} \vec{u}_{displ} \cdot (\vec{k}_{fw} - \vec{k}_{bw}) \\ &= \frac{4\pi}{\lambda} \Delta x_{az} \cdot \|\vec{j}_{diff}\| \end{aligned} \quad (A4)$$

with

$$\vec{j}_{diff} = \vec{k}_{fw} - \vec{k}_{bw} \approx \Delta\Psi_{ovl} \cdot \vec{j}_{along-track} \quad (A5)$$

where $\vec{j}_{along-track}$ is a horizontal unit vector parallel to the satellite track. In TOPS mode, the squint angle difference $\Delta\Psi_{ovl}$ between two consecutive overlaps for a given subswath can be deduced from the beam steering rate k_Ψ and the time separation between overlaps $\Delta\eta_{ovl}$

$$\Delta\Psi_{ovl} = \Delta\eta_{ovl} k_\Psi \quad (A6)$$

Typical numerical values of the above parameters for Sentinel-1 TOPS IW mode are provided in Table A1. Ultimately, the along-track displacement Δx_{az} (in centimeters) is obtained by multiplying the double-difference phase $\Delta\Phi_{ovl}$ (in radian) by a factor $\sim 21 - 25$ cm/rad, meaning that a full along-track fringe represents an along-track displacement of ~ 130 cm (for comparison, the radian-to-centimeter conversion factor is equal to ~ 0.44 cm/rad for the ~ 2.8 cm across-track fringe).

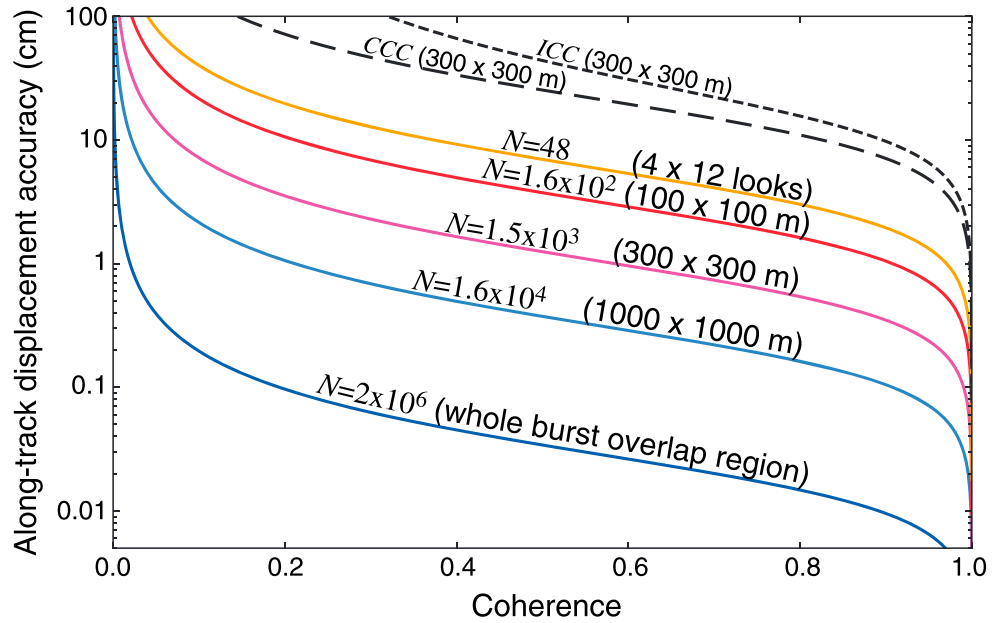


Figure A1. Theoretical accuracy of the along-track displacement achieved by Sentinel-1 burst overlap interferometry, as a function of coherence γ , for an azimuth pixel size $\Delta x_s = 14$ m (color lines, equation (A7)). Several cases are distinguished, depending on the number of full-resolution pixels N used for the averaging. The accuracy of coherent and incoherent cross-correlation techniques (respectively, CCC and ICC) at 300×300 m posting is shown for comparison (black dashed lines, equation (A8)).

A2. Uncertainty Assessment

From a signal processing point of view, the theoretical accuracy achieved by the double-difference interferogram in burst overlaps is given by the error standard deviation [Bamler and Eineder, 2005; Prats-Iraola et al., 2012]

$$\sigma_{ovl} = \frac{1}{2\pi\Delta f_{ovl}} \frac{1}{\sqrt{N}} \frac{\sqrt{1-\gamma^2}}{\gamma} \frac{1}{\Delta t_s} \tag{A7}$$

here provided in units of resolution elements. In this expression, N is the number of pixels used in the spatial averaging, γ is the coherence, and Δf_{ovl} is the spectral separation in the overlap region (~ 4 kHz for Sentinel IW). As shown in Figure A1, the expected accuracy strongly depends on the number of independent pixels used in the averaging but less so on the coherence. In case of a uniform shift across the whole burst overlap region (i.e., no deformation), N may exceed a million pixels, so that an accuracy better than 0.1 cm can be reached. However, the accuracy decreases to 0.3–1 cm if displacement changes over distances of the order of 1 km and up to 10 cm for 100 m posting in adverse coherence conditions. These estimates are in rough agreement with the residual fit to the GPS measured for the Illapel earthquake data set (RMS = 3–5 cm, section 3.2), which corresponds to relatively good coherence conditions ($\gamma > 0.5$). For comparison, the standard deviations from coherent cross correlation (CCC) [Bamler and Eineder, 2005; De Zan, 2011] and incoherent (amplitude) cross correlation (ICC) [De Zan, 2014] are, respectively,

$$\sigma_{ICC} = \sqrt{\frac{3}{2N} \frac{\sqrt{1-\gamma^2}}{\pi\gamma}}; \quad \sigma_{CCC} = \sqrt{\frac{3}{10N} \frac{\sqrt{2+5\gamma^2-7\gamma^4}}{\pi\gamma^2}} \tag{A8}$$

For a given number of averaged pixels, the performance of the present method is better, by 1 order of magnitude, than that of ICC and CCC (Figure A1).

From a practical point of view, the double-difference along-track phase is not contaminated by atmospheric phase screen, which is the main source of error for multitemporal InSAR [e.g., Zebker et al., 1997; Hanssen, 2001]. Nevertheless, SAR interferometry (whether conventional or only in burst overlap regions) being a relative measurement, it can be affected by long-spatial wavelength nuisance stemming from residual large-scale mis-registration due to geometric approximations and/or orbit errors. In burst overlap interferograms, this effect translates locally into a bias that may reach several centimeters. This bias can be mitigated by adjustment of a

planar or higher-order polynomial trend in distant regions unaffected by the tectonic signal or accounted for as an unknown during source modeling. Alternatively, external data, such as GPS, can be used to provide a reference. Interpolation between burst overlaps can also lead to aliasing of the displacement field. The induced errors depend on the smallest spatial wavelength of the deformation. In particular, a complex displacement field (e.g., induced by shallow faulting) will significantly jeopardize the validity of the interpolation.

Acknowledgments

The Sentinel-1 data used for this study are provided by ESA/Copernicus. Interferometric processing was carried out using a modified version of ROI_PAC software [Rosen *et al.*, 2004]. Most figures were designed, and some processing steps (filtering, interpolation) were performed with the help of GMT software [Wessel and Smith, 1991]. The GPS observations used in this study were acquired through the Centro Sismológico Nacional (CSN) and the French-Chilean Laboratoire International Associé (LIA) geodetic networks. This project was supported by PNTS grant "PNTS-2015-09" and by the "MEGACHILE" project funded by the Agence Nationale de la Recherche (ANR). This is the IPGP contribution 3721. We thank two anonymous reviewers whose insightful suggestions helped us to improve the manuscript.

References

- Bamler, R., and M. Eineder (2005), Accuracy of differential shift estimation by correlation and split-bandwidth interferometry for wideband and delta-k SAR systems, *IEEE Geosci. Remote Sens. Lett.*, *2*(2), 151–155.
- Barbot, S., Y. Hamiel, and Y. Fialko (2008), Space geodetic investigation of the coseismic and postseismic deformation due to the 2003 M_w 7.2 Altai earthquake: Implications for the local lithospheric rheology, *J. Geophys. Res.*, *113*, B03403, doi:10.1029/2007JB005063.
- Bechor, N. B., and H. A. Zebker (2006), Measuring two-dimensional movements using a single InSAR pair, *Geophys. Res. Lett.*, *33*, L16311, doi:10.1029/2006GL026883.
- De Zan, F. (2011), Coherent shift estimation for stacks of SAR images, *IEEE Geosci. Remote Sens. Lett.*, *8*(6), 1095–1099.
- De Zan, F. (2014), Accuracy of incoherent speckle tracking for circular gaussian signals, *IEEE Geosci. Remote Sens. Lett.*, *11*(1), 264–267.
- De Zan, F., and A. M. Guarnieri (2006), TOPSAR: Terrain observation by progressive scans, *IEEE Trans. Geosci. Remote Sens.*, *44*(9), 2352–2360.
- De Zan, F., P. Prats-Iraola, R. Scheiber, and A. Rucci (2014), Interferometry with tops: Coregistration and azimuth shifts, paper presented at 10th European Conference on Synthetic Aperture Radar, EUSAR 2014, pp. 1–4, VDE, Berlin, Germany, 3–5 Jun.
- De Zan, F., P. Prats-Iraola, and M. Rodríguez-Cassola (2015), On the dependence of delta-k efficiency on multilooking, *IEEE Geosci. Remote Sens. Lett.*, *12*(8), 1745–1749.
- Ducret, G. (2013), *Mesure de déformation par interférométrie radar: Développements méthodologiques et applications à la subduction Chilienne*, PhD thesis, Institut de Physique du Globe de Paris, France.
- Fialko, Y., M. Simons, and D. Agnew (2001), The complete (3-D) surface displacement field in the epicentral area of the 1999 M_w 7.1 Hector Mine earthquake, California, from space geodetic observations, *Geophys. Res. Lett.*, *28*(16), 3063–3066, doi:10.1029/2001GL013174.
- Goldstein, R. M., H. A. Zebker, and C. L. Werner (1988), Satellite radar interferometry—Two-dimensional phase unwrapping, *Radio Sci.*, *23*(4), 713–720.
- González, P. J., M. Bagnardi, A. J. Hooper, Y. Larsen, P. Marinkovic, S. V. Samsonov, and T. J. Wright (2015), The 2014–2015 eruption of Fogo volcano: Geodetic modeling of Sentinel-1 TOPS interferometry, *Geophys. Res. Lett.*, *42*, 9239–9246, doi:10.1002/2015GL066003.
- Grandin, R. (2015), Interferometric Processing of SLC Sentinel-1 TOPS Data, paper presented at the European Space Agency, SP-371, FRINGE 2015, Frascati, Rome, Italy, 23–27 Mar.
- Grandin, R., et al. (2009), September 2005 Manda Hararo-Dabbahu rifting event, Afar (Ethiopia): Constraints provided by geodetic data, *J. Geophys. Res.*, *114*, B08404, doi:10.1029/2008JB005843.
- Grandin, R., M. Vallée, C. Satriano, R. Lacassin, Y. Klinger, M. Simoes, and L. Bollinger (2015), Rupture process of the M_w = 7.9 2015 Gorkha earthquake (Nepal): Insights into Himalayan megathrust segmentation, *Geophys. Res. Lett.*, *42*, 8373–8382, doi:10.1002/2015GL066044.
- Hanssen, R. F. (2001), *Radar Interferometry: Data Interpretation and Error Analysis*, vol. 2, Springer, Netherlands.
- Holzner, J., and R. Bamler (2002), Burst-mode and ScanSAR interferometry, *IEEE Trans. Geosci. Remote Sens.*, *40*(9), 1917–1934.
- Jung, H.-S., J.-S. Won, and S.-W. Kim (2009), An improvement of the performance of multiple-aperture SAR interferometry (MAI), *IEEE Trans. Geosci. Remote Sens.*, *47*(8), 2859–2869.
- Jung, H.-S., W.-J. Lee, and L. Zhang (2014), Theoretical accuracy of along-track displacement measurements from Multiple-Aperture Interferometry (MAI), *Sensors*, *14*(9), 17,703–17,724.
- Jung, H.-S., Z. Lu, A. Shepherd, and T. Wright (2015), Simulation of the SuperSAR multi-azimuth synthetic aperture radar imaging system for precise measurement of three-dimensional Earth surface displacement, *IEEE Trans. Geosci. Remote Sens.*, *53*(11), 6196–6206.
- Melgar, D., W. Fan, S. Riquelme, J. Geng, L. Liang, M. Fuentes, G. Vargas, R. Allen, P. Shearer, and E. Fielding (2016), Slip segmentation and slow rupture to the trench during the 2015, M_w 8.3 Illapel, Chile earthquake, *Geophys. Res. Lett.*, *43*, 961–966, doi:10.1002/2015GL067369.
- Meta, A., P. Prats, U. Steinbrecher, J. Mittermayer, and R. Scheiber (2008), TerraSAR-X TOPSAR and ScanSAR comparison, presented at 7th European Conference on Synthetic Aperture Radar (EUSAR), pp. 1–4, VDE, Friedrichshafen, Germany, 2–5 Jun.
- Michel, R., J.-P. Avouac, and J. Taboury (1999), Measuring ground displacements from SAR amplitude images: Application to the Landers earthquake, *Geophys. Res. Lett.*, *26*, 875–878, doi:10.1029/1999GL900138.
- Mittermayer, J., S. Wollstadt, P. Prats-Iraola, P. López-Dekker, G. Krieger, and A. Moreira (2013), Bidirectional SAR imaging mode, *IEEE Trans. Geosci. Remote Sens.*, *51*(1), 601–614.
- Peltzer, G., F. Crampé, and G. King (1999), Evidence of nonlinear elasticity of the crust from the M_w 7.6 Manyi (Tibet) earthquake, *Science*, *286*(5438), 272–276.
- Prats-Iraola, P., R. Scheiber, L. Marotti, S. Wollstadt, and A. Reigber (2012), TOPS interferometry with TerraSAR-X, *IEEE Trans. Geosci. Remote Sens.*, *50*(8), 3179–3188.
- Pritchard, M., C. Ji, and M. Simons (2006), Distribution of slip from 11 M_w > 6 earthquakes in the northern Chile subduction zone, *J. Geophys. Res.*, *111*, B10302, doi:10.1029/2005JB004013.
- Rosen, P. A., S. Henley, G. Peltzer, and M. Simons (2004), Updated repeat orbit interferometry package released, *Eos Trans. AGU*, *85*(5), 47–47, doi:10.1029/2004EO050004.
- Scheiber, R., and A. Moreira (2000), Coregistration of interferometric SAR images using spectral diversity, *IEEE Trans. Geosci. Remote Sens.*, *38*(5), 2179–2191.
- Scheiber, R., M. Jager, P. Prats-Iraola, F. De Zan, and D. Geudtner (2015), Speckle tracking and interferometric processing of TerraSAR-X TOPS data for mapping nonstationary scenarios, *IEEE J. Sel. Top. Appl. Earth Obs. Remote Sens.*, *8*(4), 1709–1720.
- Simons, M., and P. Rosen (2007), Interferometric synthetic aperture radar geodesy, *Treatise Geophys.*, *3*, 391–446.
- Torres, R., et al. (2012), Gmes Sentinel-1 mission, *Remote Sens. Environ.*, *120*, 9–24.
- Wessel, P., and W. H. F. Smith (1991), Free software helps map and display data, *Eos Trans. AGU*, *72*, 441–441, doi:10.1029/90EO00319.
- Wright, T. J., B. E. Parsons, and Z. Lu (2004), Toward mapping surface deformation in three dimensions using InSAR, *Geophys. Res. Lett.*, *31*, L01607, doi:10.1029/2003GL018827.
- Zebker, H. A., P. A. Rosen, and S. Hensley (1997), Atmospheric effects in interferometric synthetic aperture radar surface deformation and topographic maps, *J. Geophys. Res.*, *102*(B4), 7547–7563.